Measurement 248 (2025) 116983

Contents lists available at ScienceDirect

Measurement

journal homepage: www.elsevier.com/locate/measurement

The detection of seawater elements by virtual polarizer capable of coherent perfect ultra-wideband polarization control

Chuan-Qi Wu [a], You-ran Wu [a], Hai-Feng Zhang [a,b,*]

[a] College of Electronic and Optical Engineering & College of Flexible Electronics (Future Technology), Nanjing University of Posts and Telecommunications, Nanjing 210023, China
[b] State Key Laboratory of Millimeter Waves of Southeast University, Nanjing 210096, China

ARTICLE INFO

Keywords:
Virtual polarizer
Coherent perfect polarization conversion
Seawater element detection
Ultra-Wideband modulation

ABSTRACT

Recently, the significance of monitoring seawater quality has gradually increased due to the sharp increase in marine pollution due to human activities. A virtual polarizer (VP) capable of detecting seawater elements, is proposed in this paper. Coherent perfect polarization control over ultra-wideband can be achieved by manipulating two coherent electromagnetic waves (EWs). The detection of salinity and volume fraction of heavy oil of seawater can be realized by observing the perfectly matched points. Within 18.55 ~ 23.88 THz, coherent polarization conversion is realized with an extremely high polarization conversion rate, which performs a vital function in controlling the propagation of EWs. Meanwhile, under TM mode, coherent perfect absorption (CPA) is achieved with a high-quality factor, which utilizes phase modulation to enable the detection of seawater algal content, and temperature. Utilizing the fragility of CPA, detecting schemes implemented employing this mechanism enable high sensitivity and low detection errors. In addition, the sensitivity, quality factor, figure of merit, and detection limit will be particularly emphasized by the calculation of the transfer matrix method. As a multifunctional instrument, the VP maintains excellent polarization conversion performance and detecting properties, offering promising applications in antenna sensing and propagation. Furthermore, the proposed VP is only a theoretical study and experimentation is not the focus of this paper.

1. Introduction

The phenomenon known as interference occurs often in the circumstance of several overlapping coherent waves, where the energy in space will be redistributed [1]. Several devices, such as spectrometers, interferometers, and antennas, rely on this fundamental principle to function. By tuning the loss rates introduced into the structure to achieve critical coupling, the resonator can completely absorb incoming electromagnetic waves (EWs) without scattering, which can be called coherent perfect absorption (CPA) [2,3]. The theoretical foundation of CPA is rooted in the time-reversal process of laser emission, which has a close connection with time-reversal symmetry [3,4]. The effective description and prediction of CPA rely on the utilization of the scattering matrix. This approach reveals that CPA tends to occur on frequency bands with small bandwidths, as the eigenvalue of the scattering matrix must be zero for CPA to take place [5]. Indeed, achieving CPA requires careful selection of the system setup and configurations. Given that CPA is extremely sensitive to minor changes in the parameters of detected samples, precise tuning and control of the experimental setup are crucial to realizing CPA in practical applications [3,4]. Significantly, the all-optical extraordinary wavelength control does not depend on nonlinear phenomena. CPA goes beyond Ohmic absorption and finds application in various other energy conversion processes, such as storage, polarization conversion, diffraction, and fluorescence [6–10]. In 2015, Mousavi et al. controlled the optical effects (birefringence, optical activity) using a coherent wave interacting with polarization in sub-wavelength thin of linear material [6]. In 2015, Kang et al. introduced a mechanism wherein a metamaterial surface, or metasurface, operates as a perfect phase-controlled rotatable linear polarizer [7]. In 2020, Mohammad et al. proposed a dual-band polarization converter designed on a single-layer substrate that converts input LPWs into output CPWs, which can be described as a utility model relating to a high-gain dual-band transmit array feed power supply [11]. However, none of their previous work utilized the coherent perfect polarization conversion (CPPC) mechanism. CPPC is a conservative and reversible optical mode conversion process that operates as a multiport system, achieving

* Corresponding author.
E-mail addresses: b22021517@njupt.edu.cn (C.-Q. Wu), yr.wu1017@gmail.com (Y.-r. Wu), hanlor@163.com (H.-F. Zhang).

https://doi.org/10.1016/j.measurement.2025.116983
Received 23 October 2024; Received in revised form 16 December 2024; Accepted 6 February 2025
Available online 8 February 2025

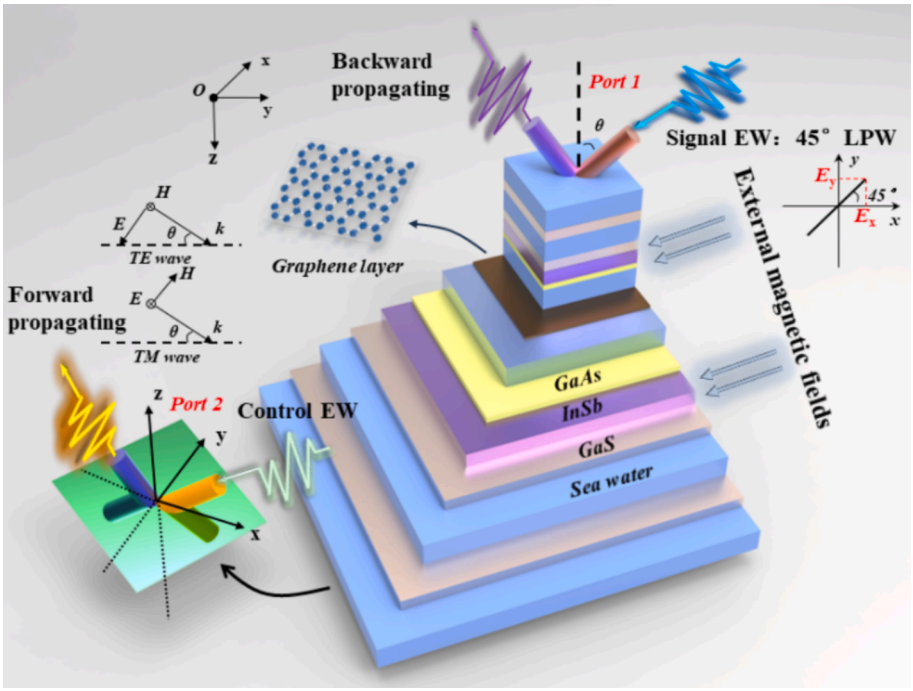

Fig. 1. The proposed VP configuration. At an angle θ, the signal waves and control waves are both incidents obliquely, occurring simultaneously in both the forward and backward directions.

maximal efficiency. It stands as a counterpart to the coherent perfect absorber in terms of phenomenological correspondences. Both CPPC and CPA share similarities in their efficiency and coherent nature, making them important phenomena in the field of optical mode manipulation and control. In this article, options for implementing detecting using CPA and CPPC principles are discussed. Structures that can simultaneously accomplish this function are known as virtual polarizers (VPs).

The manipulation of the polarization nature of EWs carries immense importance in diverse applications, including optics and various imaging processes [12–15]. EWs, as vectorial, exhibit several polarization states, including linear, circular, and elliptical. [13]. The capacity to regulate and control polarization has created intriguing potential for applications and technology [16,17]. Wu *et al.* designed a photonic crystal containing hyperbolic metamaterials [18], which can realize the wide-angle polarization selectivity based on anomalous defect mode. Zagaglia *et al.* researched Polarization states and far-field optical properties in dielectric photonic crystal slabs [19], illustrating the relation between the topological singularities and the circular dichroism in reflectivity. She *et al.* presented a one-dimensional photonic crystal containing elliptical metamaterials [20], which has the characteristic of tunable wide-angle high-efficiency polarization selectivity. In 2024, VP, as a way for coherent wave polarization manipulation, was first proposed [21]. Different from physics polarizers, VP enabling CPPC can control the polarization nature of waves in coherent form in a two-port system. If the input is only available at one port, despite the structure's existence, the desired polarization effect cannot be achieved using the VP. Similar to the formation mechanism of CPA, VP can realize CPPC under the influence of a standing wave. CPPC shared the fragile nature with the CPA. In homogeneous dielectric, local energy standing wave can be found in the structure, under which circumstance, the VP shows no ability to manipulate the polarization of coherent wave and the local polarization form is unchanged along the wave axes. However, due to the anisotropic evolution, the energy standing wave in the local energy density envelope turns into the polarized standing wave, and the various local polarization forms appear at the different positions of the axis. During the evolution, the standing wave is sensitive to the configuration of the VP. Hence, it is possible to use a perfectly matched point (PMP) for detection, where the definition of the PMP is the frequency point corresponding to the axial ratio (AR) of 0 dB when the EWs are circular polarization waves [21]. Together with CPA detecting, the VP enables versatile, highly sensitive detection.

The importance of pollution detection of seawater cannot be overstated, as it makes a great difference in marine life, and ultimately, our planet. The presence of heavy oil in seawater poses significant dangers. When heavy oil spills occur in the ocean, the oil tends to spread quickly and form thick, sticky slicks on the surface. These spills can coat beaches, rocks, and shorelines, leading to long-lasting environmental damage. Meanwhile, the presence of certain types of algae in seawater can lead to harmful algal blooms, which pose significant dangers to marine ecosystems, human health, and coastal economies. The detection of salinity and temperature in seawater is crucial for understanding ocean circulation, climate patterns, marine ecosystems, and weather prediction. It also helps monitor ocean health, and pollution and supports maritime operations. VP utilizes CPPC to achieve seawater detection with higher accuracy due to the better immunity to the interference of circular polarization. Therefore, VP has a great role in detecting marine ecosystems and is of wide application. Recently, there have been some studies conducted on the detection of seawater ecosystems. In 2018, Vigneswaran et al. proposed a fiber based on photonic crystals for monitoring seawater salinity, whose sensitivity (S) is high to 5675 nm/RIU [22]. In 2020, Mollah et al. studied a photonic crystal fiber based on a Sagnac interferometer for salinity detection, achieving an S of 7.5 nm/% [23]. In 2020, Zhu et al. proposed a cavity resonator, which can result in multiple fano resonances with the asymmetry of the T-shaped cavity changed. The S of the sensor is up to 1066 nm/RIU [24]. In 2023, Zhai et al. proposed a way to detect seawater temperature by incorporating the three interferometers with the bow tie fiber. Based on the experiment, the structure obtained an S of 1.19 nm/K [25]. However, previous work has been limited to the detection of a single nature. Compared with the previous work, the VP proposed in this paper can measure more physical quantities, is more comprehensive in measuring various seawater parameters, and possesses higher sensitivity. In addition, the VP enables controlling coherent EWs, making it a versatile device. The use of different principles of measurement increases the

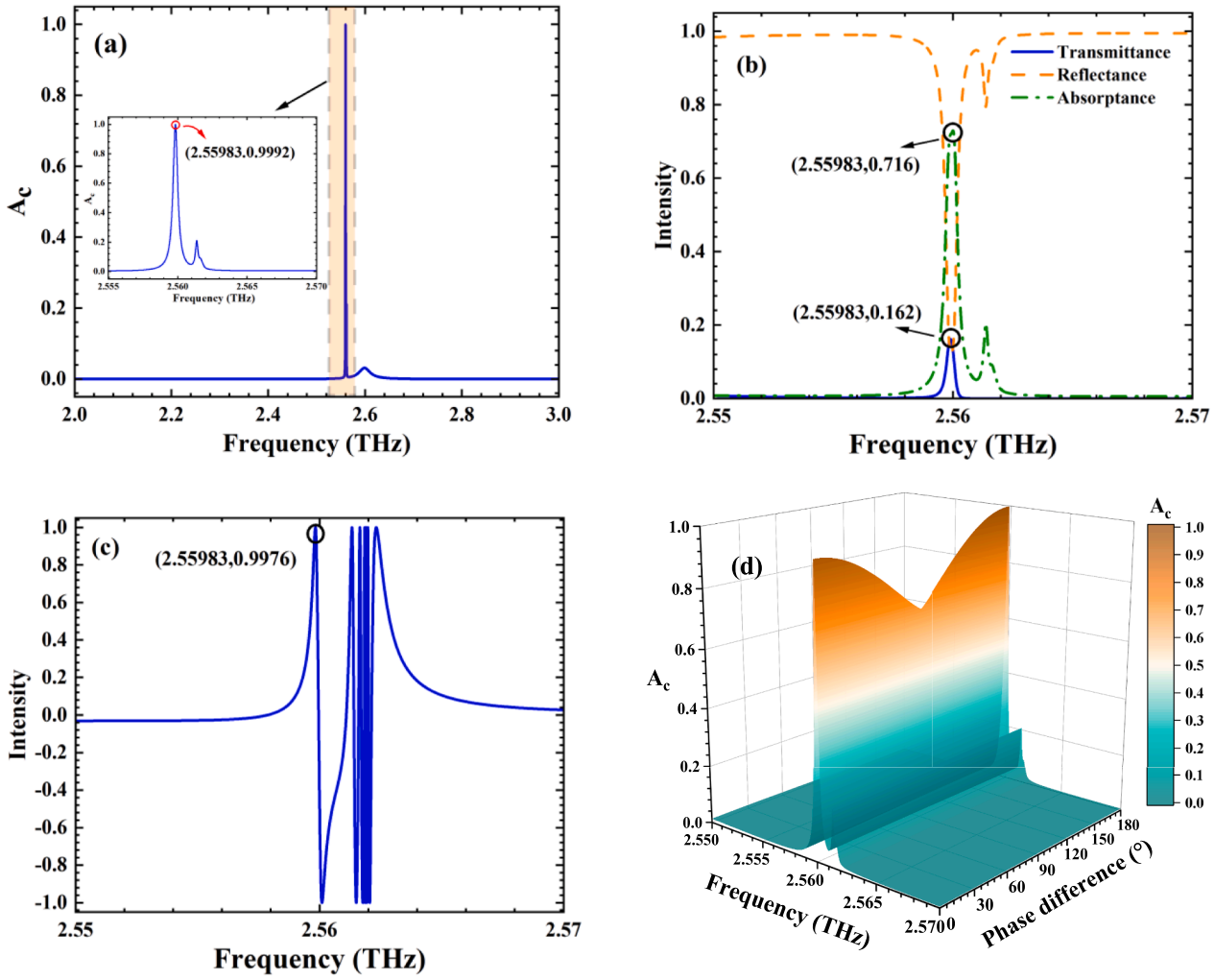

Fig. 2. **(a)** The relationship between the absorption and the frequency of EWs When CPA is realized by the proposed VP. **(b)** The curves of the reflection and transmission in the case that EWs incident one side. **(c)** The $\cos\varphi_1$ must be equal to -1 or 1 with the realization of CPA. **(d)** The three-dimensional diagram reveals the connection between the phase difference of two coherent incident waves and the absorption.

adaptability of the VP.

In this work, a novel innovation point, VP, which is based on a Parity-time (PT)-symmetric structure, is proposed. VP not only controls the polarization of EWs but also detects marine ecological conditions with high precision. The structure can emit two EWs with distinct polarization states that are mutually chiral to each other by manipulating both the chiral control EWs and signal EWs. Within 18.55 ~ 23.88 THz, CPPC is realized with an extremely high polarization conversion rate (*PCR*), utilizing the PMP enables the detection of salinity and volume fraction of heavy oil. Meanwhile, under TM mode, CPA is achieved with a high sensitivity, which utilizes phase modulation to enable the detection of temperature and seawater algal concentration. The proposed VP owns two detection modes, PMP and CPA, which can be freely switched according to the needs of detection. For the VP, it is the first time to present the way of PMP detection, enlarging the function range of the VP and revealing a new method to combine polarization conversion with detection [21]. Furthermore, With the combination of PMP and CPA, the VP takes advantage of multiple physical quantities detection in seawater, which not only enriches the detection methods of seawater elements but also owns the potential for multi-scenario application. Unfortunately, due to the lack of appropriate experimental conditions, this paper mainly focuses on the theoretical feasibility of the VP, and experimentation is not the focus of this paper.

2. Models and theories

The operational principle of the designed VP is carefully illustrated in Fig. 1. The whole VP is composed of dielectrics indium antimonide (InSb), gallium arsenide (GaAs) [26], Gallium sulfide (GaS) [27], graphene layer (GL), and a cavity (C) filled with seawater for determination, and its PT symmetrical structural arrangement belongs to (C-GaS-C-GaS) (InSb-GaAs-C-GL-C-GaAs-InSb) (GaS-C-GaS-C). For simplicity, the same medium layers have the same thickness. The $+z$-direction experiences the incident of the signal wave in the forward direction, whereas the control wave incidents backward along the $-z$-direction at an angle θ. Two counter-propagating waves interfere with each other and CPPC is generated. When the outgoing EW is emitted from port 2 of VP (see Fig. 1), the EW propagating along the $+z$-direction can be referred to as forward-propagating, while the one moving in the opposite direction ($-z$) can be termed as backward-propagating EW.

The refractive indexes (RIs) of the GaAs, and GaS, are, $n_{GaAs} = 3.43$ [26], and $n_{GaS} = 2.45$ [27], respectively, and the thicknesses are in sequence $d_{GaAs} = 0.9$ μm, $d_{GaS} = 1.7$ μm, respectively. Besides, the thicknesses of Seawater and InSb are $d_{Seawater} = 3.5$ μm and $d_{InSb} = 2.37$ μm, respectively.

Owing to that InSb, affected by the external magnetic field, will show anisotropy in the terahertz (THz) band, the dielectric constant tensor of InSb has been defined as [5]:

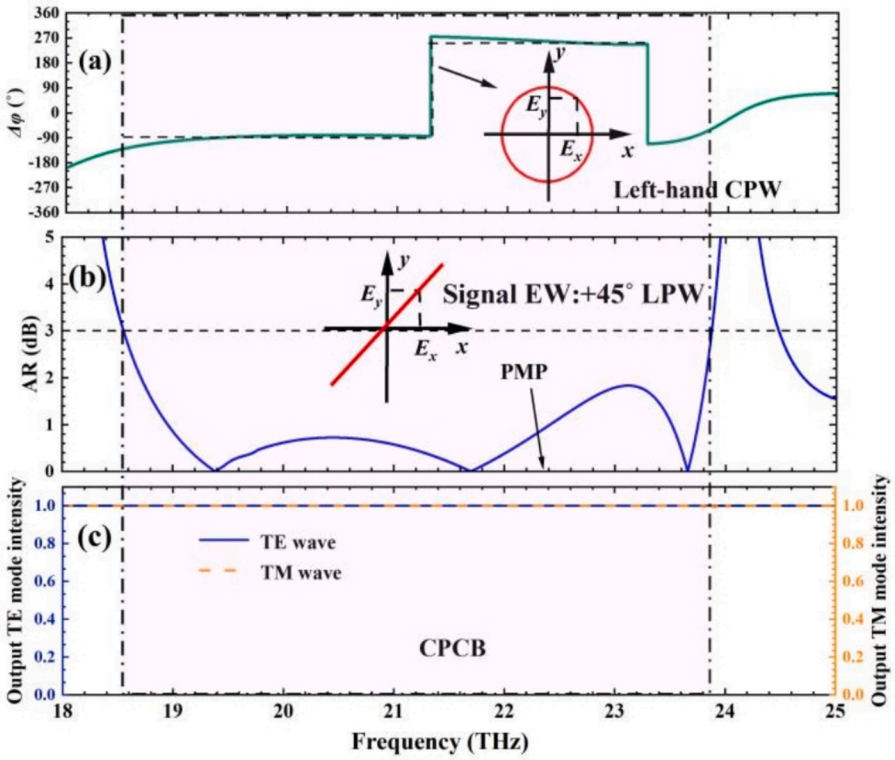

Fig. 3. Output intensities and polarization characteristics of VP in 18 ~ 25 THz. **(a)** The variation of phase difference $\Delta\varphi$ with frequency, **(b)** Variation of the AR with frequency, **(c)** Output characteristics of VP in the operating frequency band.

$$\varepsilon_{\mathrm{InSb}} = \begin{pmatrix} \varepsilon_x & 0 & i\varepsilon_{xz} \\ 0 & \varepsilon_y & 0 \\ -i\varepsilon_{xz} & 0 & \varepsilon_x \end{pmatrix} \tag{1}$$

where

$$\varepsilon_x = \varepsilon_\infty - \varepsilon_\infty \frac{\omega_p^2(\omega + i\nu_c)}{\omega\left[(\omega + i\nu_c)^2 - \omega_c^2\right]} \tag{1a}$$

$$\varepsilon_y = \varepsilon_\infty - \varepsilon_\infty \frac{\omega_p^2}{\omega(\omega + i\nu_c)} \tag{1b}$$

$$\varepsilon_{xz} = \varepsilon_\infty \frac{-\omega_p^2\omega_c}{\omega\left[(\omega + i\nu_c)^2 - \omega_c^2\right]} \tag{1c}$$

Herein, ε_∞=15.68 is on behalf of the high-frequency permittivity and $\omega_p=(e^2N/\varepsilon_0\varepsilon_\infty m^*)^{1/2}$ stands for the plasma frequency, $\nu_c = 0.00008\omega_p$ represents the carrier collision frequency, and $\omega_c = eB/m^*$ is defined as the cyclotron frequency, related to the external magnetic field [5]. The magnetic field strength B is fixed as 0.34 T, $\omega = 2\pi f$ stands for the angle frequency, while f refers to the frequencies of EWs. ε_0 is equal to the vacuum dielectric constant and e is deemed as the electronic power. m denotes the electronic quality and m^*=0.015 m. N, for a given temperature T (296 K, typically), is the intrinsic carrier density, which is expressed as [5]:

$$N = 5.76 \times 10^{20} T^{1.5} \exp\left[-0.26/\left(2 \times 8.625 \times 10^{-5} \times T\right)\right] \tag{2}$$

When the EWs appear as TE and TM waves, the dielectric constants and transfer matrices of Insb are defined as follows [28]:

$$\varepsilon_{\mathrm{InSb(TE)}} = \varepsilon_y \tag{3a}$$

$$\varepsilon_{\mathrm{InSb(TM)}} = \frac{\varepsilon_x^2 - \varepsilon_{xz}^2}{\varepsilon_x} \tag{3b}$$

$$\mathrm{M}_{InSb(TE)} = \begin{bmatrix} \cos(\mathrm{k_{1z}d}_{InSb}) & -\frac{\mathrm{i}}{\eta_1}\sin(\mathrm{k_{1z}d}_{InSb}) \\ -\mathrm{i}\eta_1\sin(\mathrm{k_{1z}d}_{InSb}) & \cos(\mathrm{k_{1z}d}_{InSb}) \end{bmatrix} \tag{3c}$$

$$\mathrm{M}_{InSb(TM)} = \begin{bmatrix} \cos(\mathrm{k_{2z}d}_{InSb}) + \frac{\mathrm{k_{2x}}\varepsilon_{xz}}{\mathrm{k_{2z}}\varepsilon_x}\sin(\mathrm{k_{2z}d}_{InSb}) & -\frac{\mathrm{i}}{\eta_2}\left[1 + \left(\frac{\mathrm{k_{2x}}\varepsilon_{xz}}{\mathrm{k_{2z}}\varepsilon_x}\right)^2\right]\sin(\mathrm{k_{2z}d}_{InSb}) \\ -\mathrm{i}\eta_2\sin(\mathrm{k_{2z}d}_{InSb}) & \cos(\mathrm{k_{2z}d_{InSb}}) - \frac{\mathrm{k_{2x}}\varepsilon_{xz}}{\mathrm{k_{2z}}\varepsilon_x}\sin(\mathrm{k_{2z}d}_{InSb}) \end{bmatrix} \tag{3d}$$

where k_{1z}, k_{2z}, and k_{2x} stand for the wave vectors of TE or TM waves along the $+x$ and $+z$ axes, respectively, which can be calculated from [28].

Considering a GL with a thickness d_G of 0.34 nm, what is possible is

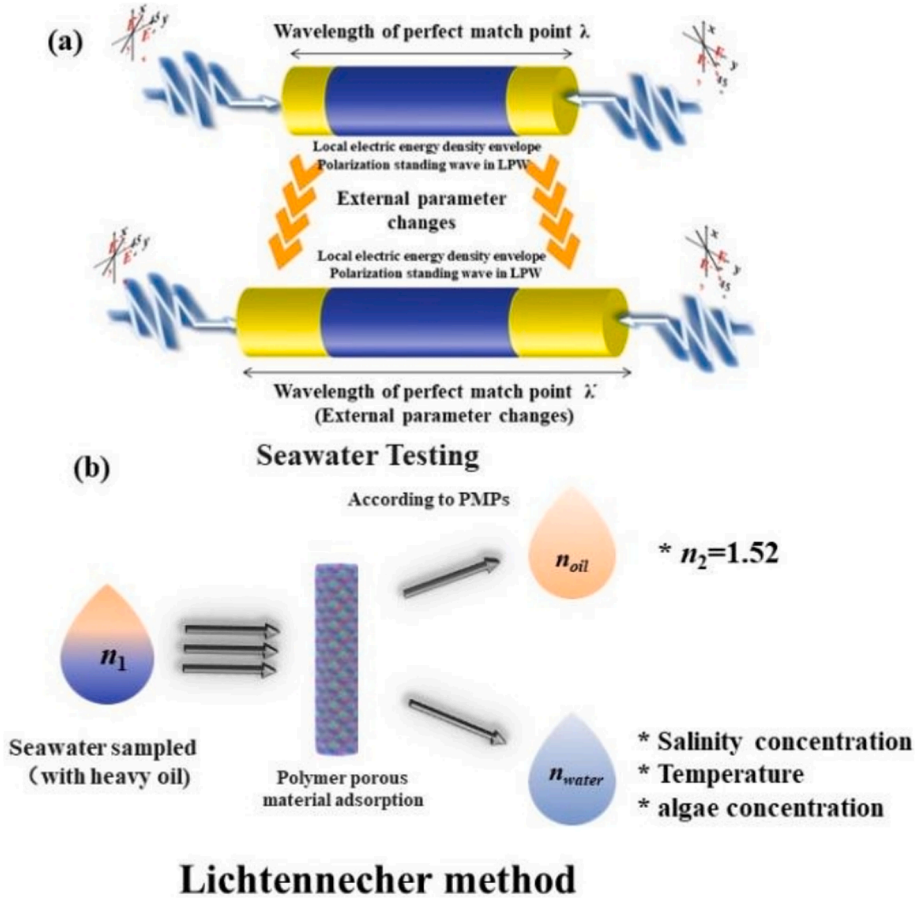

Fig. 4. (a) The polarization standing wave and the relationships between external parameters and the wavelength(frequency) of the PMP. (b) Seawater detection procedure using the principle of CPPC [31].

that the chemical potential μ_c of GLs can be modulated by regulating the external voltage.

The surface conductivity σ is associated with the GL and consists of both intraband conductivity σ_{intra}, and interband conductivity σ_{inter} [29].

$$\sigma = \frac{ie^2 k_B T}{\pi\hbar^2(\omega + i/\tau)}\left(\frac{\mu_C}{k_B T} + 2\ln\left(e^{-\frac{\mu_C}{k_B T}} + 1\right)\right) + \frac{ie^2}{4\pi\hbar}\ln\left(\frac{2|\mu_C| - \hbar(\omega + i/\tau)}{2|\mu_C| + \hbar(\omega + i/\tau)}\right)\Bigg) \tag{4}$$

where $\hbar$, k_B, τ are Planck constant, Boltzmann constant, and relaxation time in turn. Relaxation time τ is set to 0.1 ps [29]. T is 296 K as mentioned above and μ_C is fixed as 0.8 eV. In the absence of any influence from adjacent elements on the electronic band structure of GL, the effective dielectric constant ε_G can be expressed below [29]:

$$\varepsilon_G = 1 + \frac{i\sigma}{\omega\varepsilon_0 d_G} \tag{5}$$

For the TE and TM waves, the transfer matrices of GaS, GaAs, C, and GL are written as follows [28]:

$$M_q = \begin{bmatrix} \cos(k_{qz}d_q) & -\frac{i}{\eta_q}\sin(k_{qz}d_q) \\ -i\eta_q\sin(k_{qz}d_q) & \cos(k_{qz}d_q) \end{bmatrix} \tag{6}$$

where q can be on behalf of GaS, GaAs, C, and GL. Moreover, kqz stands for the vector of TE and TM waves along the $+z$ axis, which can be attained from [28].

The transfer matrix method (TMM) can be applied to calculate the energy communication between layers [5].

$$M_{\text{Total}} = \prod_{i=1}^{N} M_i \tag{7}$$

The R_c and T_c are denoted as the reflection and transmission, which can be obtained by the reflection coefficient r and transmission coefficient t. The formulas are described as follows [5]:

$$R_c = |r|^2 \tag{8}$$

$$T_c = |t|^2 \tag{9}$$

where

$$r = \frac{(m_{11} + m_{12}\eta_{N+1})\eta_0 - (m_{21} + m_{22}\eta_{N+1})}{m_{11}\eta_0 + m_{12}\eta_0\eta_{N+1} + m_{21} + m_{22}\eta_{N+1}} \tag{10}$$

$$t = \frac{2\eta_0}{m_{11}\eta_0 + m_{12}\eta_0\eta_{N+1} + m_{21} + m_{22}\eta_{N+1}} \tag{11}$$

The η_1, η_2, η_q, η_0, and η_{N+1} are on behalf of the admittance of TE or TM waves under different media. The proposed VP is placed in the vacuum. So, to simplify the definitions of the admittance about TE and TM waves, they will be shown as generic forms [28]:

$$\eta_{TE} = \sqrt{\frac{\varepsilon_0\varepsilon_e}{\mu_0\mu_e}}\cos(\theta_e) \tag{12}$$

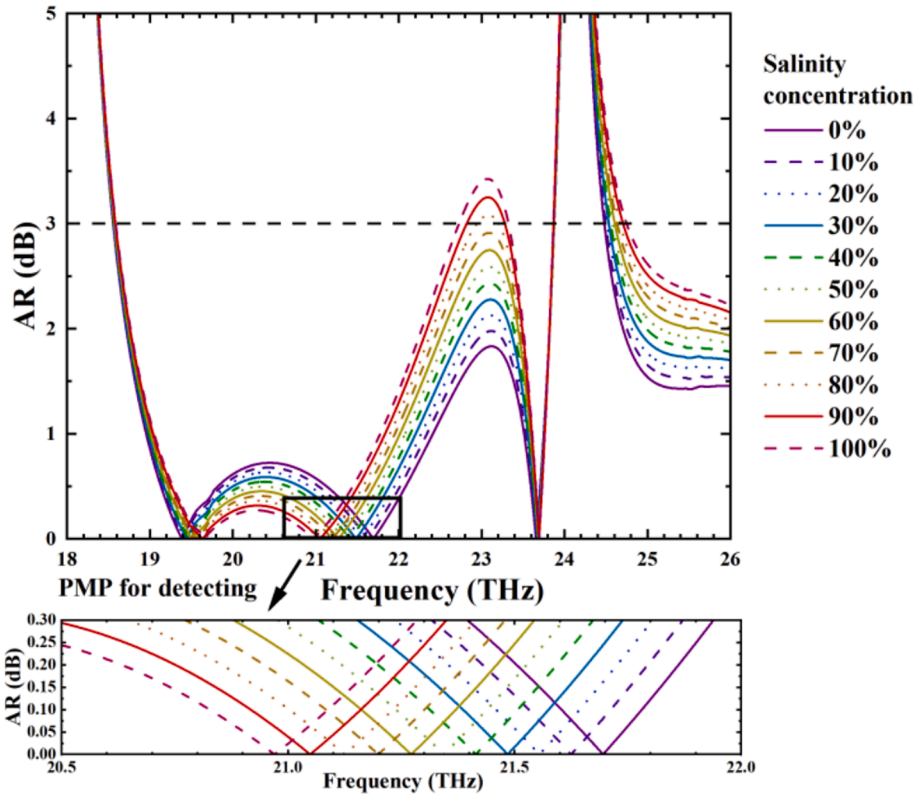

Fig. 5. Curves of AR versus frequency at different salinity concentrations (from 0 % to 100 %), and shifting trend of PMP.

$$\eta_{TM} = \sqrt{\frac{\varepsilon_0 \varepsilon_e}{\mu_0 \mu_e}} \frac{1}{\cos(\theta_e)} \tag{13}$$

where ε_0 and μ_0 are defined as the permittivity and permeability in vacuum, respectively. Furthermore, ε_e, μ_e, and θ_e are on behalf of the relative permittivity, relative permeability, and incidence angle when EWs propagate in a particular medium.

When two counter-propagating EWs encounter, the scattering electromagnetic fields (O_+ and O_-) in the forward and backward can be derived from the incident waves (I_+ and I_-) in the forward and backward, respectively, which can be denoted as follows [5]:

$$\begin{pmatrix} O_+ \\ O_- \end{pmatrix} = S \begin{pmatrix} I_+ \\ I_- \end{pmatrix} = \begin{pmatrix} t & r \\ r & t \end{pmatrix} \begin{pmatrix} I_+ \\ I_- \end{pmatrix} \tag{14}$$

The phase difference between the incident waves is assumed as $\Delta\Phi$, equally, the formula (14) can be written as [5]:

$$O_+ = t|I_+| + r|I_-|e^{i\Delta\Phi} \tag{14a}$$

$$O_- = r|I_+| + t|I_-|e^{i\Delta\Phi} \tag{14b}$$

The φ_{TM} and, φ_{TE} are on behalf of the phases of the TM and TE wave, respectively, and thus $\Delta\varphi = \varphi_{TM} - \varphi_{TE}$ can be used to describe the phase difference between the TM and TE waves.

The coherent absorptance may be expressed as follows: [5]:

$$O_{TE(TM),(\pm)} = |O_\pm|^2 \tag{15}$$

Combining Eqs. (11a), (11b), and (12), it is attainable that [5]:

$$A_c = 1 - (|t| - |r|)^2 - 2|t||r|\left(1 + \frac{2|I_+||I_-|\cos\Delta\varphi_1 \cos\Delta\Phi}{|I_+|^2 + |I_-|^2}\right) \tag{16}$$

where $\Delta\varphi_1$ = Arg(t)-Arg(r), with the argument principal value of the plural obtained by the Arg(). To actualize CPA, the following requirements must be met [5]: (1) $|I_+| = |I_-|$, (2) $\cos\Delta\varphi_1 \cos\Delta\Phi = -1$, (3) $|t| = |r|$.

Thus, the AR is a measuring metric used to characterize polarization in EWs [21]. It provides perspective into the ellipticity or circularity of a wave's polarization state [18]. The AR is defined as the polarization ellipse's major-minor axis ratio. Evaluation of the AR offers important details about the polarization properties of waves. The AR that establishes the polarization mode of EW may be found as follows. [29,30]:

$$AR = \left(\frac{|O_{TE}|^2 + |O_{TM}|^2 + \sqrt{a}}{|O_{TE}|^2 + |O_{TM}|^2 - \sqrt{a}}\right)^{\frac{1}{2}} \tag{17}$$

where

$$a = |O_{TE}|^4 + |O_{TM}|^4 + 2|O_{TE}|^2|O_{TM}|^2\cos(2\Delta\varphi) \tag{17a}$$

$$O_{TE(TM),(\pm)} = |O_\pm|^2 \tag{17b}$$

In general, the specific polarization form of the EWs can be estimated by the AR and $\Delta\varphi$ of EWs. The AR of CPWs is usually considered to be less than 3 dB, while the AR of LPWs potentially tends to infinity.

Because the detecting function of the VP is investigated in this article, only the forward propagating output EW is examined. For the forward propagating output circular polarization waves (CPWs), $\Delta\varphi$ = -90°±360°n (n = 0, 1, 2···) indicates right-hand CPWs, and $\Delta\varphi$ = 90° ±360°n (n = 0, 1, 2···) represents left-hand CPWs. When $\Delta\varphi$ falls within the range of ± 180°±180°n (n = 0, 1, 2···), they are considered linear polarization waves (LPWs) [21]. Meanwhile, when $\Delta\varphi$ can take on any value, it is recognized as elliptically polarized waves (EPWs).

In this study, the polarization conversion is mostly accomplished through the influence of coherence, therefore the effect of cross-polarization is tiny and has little impact on the results, and hence the *PCR* may be characterized as [21]:

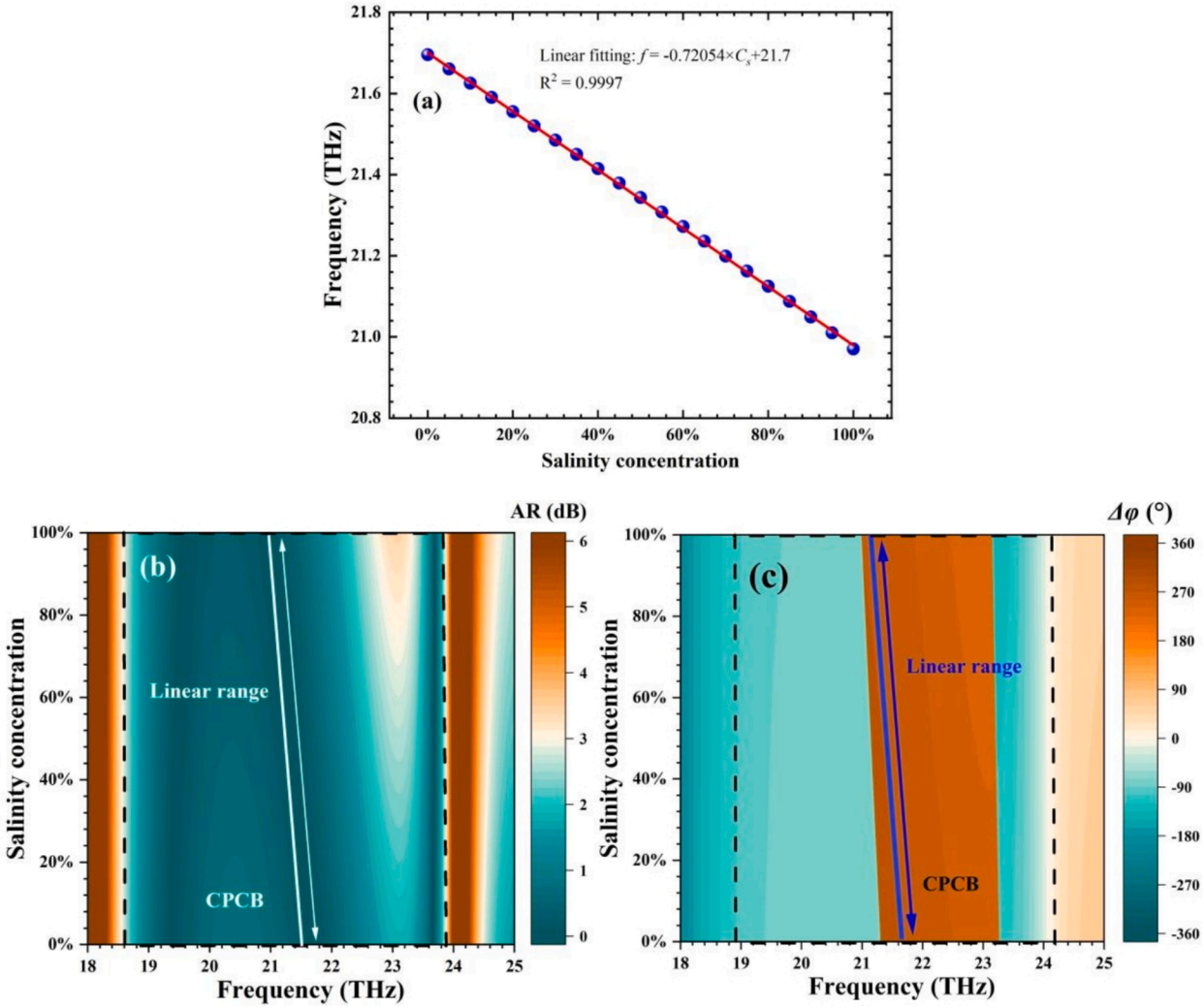

Fig. 6. VP performance in C_s detecting. **(a)** The linear fitting curve for the salinity concentration and frequency. **(b)** Effects of changes AR with different Cs. **(c)** Effects of changes in phase difference $\Delta\varphi$.

$$PCR = \frac{|O_{TE,+}|^2 + |O_{TM,+}|^2 + |O_{TE,-}|^2 + |O_{TM,-}|^2}{|I_{TE,+}|^2 + |I_{TM,+}|^2 + |I_{TE,-}|^2 + |I_{TM,-}|^2} \tag{18}$$

When the VP is used to detect the seawater elements, it is indispensable to apply S, quality (Q) factor, figure of merit (FOM^*), and detection limit (DL) to evaluate the performance of the VP. A sensor that exhibits outstanding performance will inherently possess higher values of Q, S, and FOM^*, along with a lower value of DL. The definitions, modulated to regulate absorption, are deemed below, where f_T is defined as the resonance frequency, and the full width at half maximum ($FWHM$) is thought of as the half-height breadth of the absorption peak [5].

$$S = \begin{cases} \dfrac{\Delta f}{\Delta n} \text{ for CPPC \& CPA detection (frequency modulation)} \\ \dfrac{\Delta \Phi}{\Delta n} \text{ for CPA detection (phase modulation)} \end{cases} \tag{19}$$

$$Q = \frac{f_T}{FWHM} \tag{20}$$

$$FOM^* = \left(\frac{(dI/I)}{dn}\right)_{\max} \tag{21}$$

$$DL = \frac{f_T}{20 \cdot S \cdot Q} \tag{22}$$

3. Analysis and discussion

3.1. The implementation of CPPC and CPA

The transmission characteristics of the VPs are calculated by TMM, based on the structural arrangement specified earlier (see Section II). As shown in Fig. 2(a), at the frequency of 2.55983 THz, an exceptionally narrow absorption band is observed, with the absorption peak reaching 0.9992. This remarkable absorption phenomenon can be identified as CPA. Notably, only this one absorption peak of CPA occurs in the frequency range 0 ~ 100 THz, demonstrating the potential of CPA for detecting applications. Furthermore, the absorption peak exhibits an exceptionally sharp profile, with a $FWHM$ bandwidth of 0.00055 THz. This narrow bandwidth results in a high Q factor exceeding 4654.24. Because of this unique characteristic, CPA, approaching 100 %, can be fulfilled by the designed VP at the resonance. As illustrated in Fig. 2(b), the condition of CPA is satisfied, at this point, reflection and transmission are equal, and approximately 0.16, and as shown in Fig. 2(c) the $\cos\Delta\varphi_1$ is equal to −1. In addition, the modulation of the A_c of the resonant frequency can be realized by regulating the phase difference between the two coherent EWs, which is demonstrated in Fig. 2(d). Therefore, the detection of phase modulation can be realized according to this principle of phase modulation compensated absorption. It can be found that around the A_c of 0.8, the most significant fluctuation in

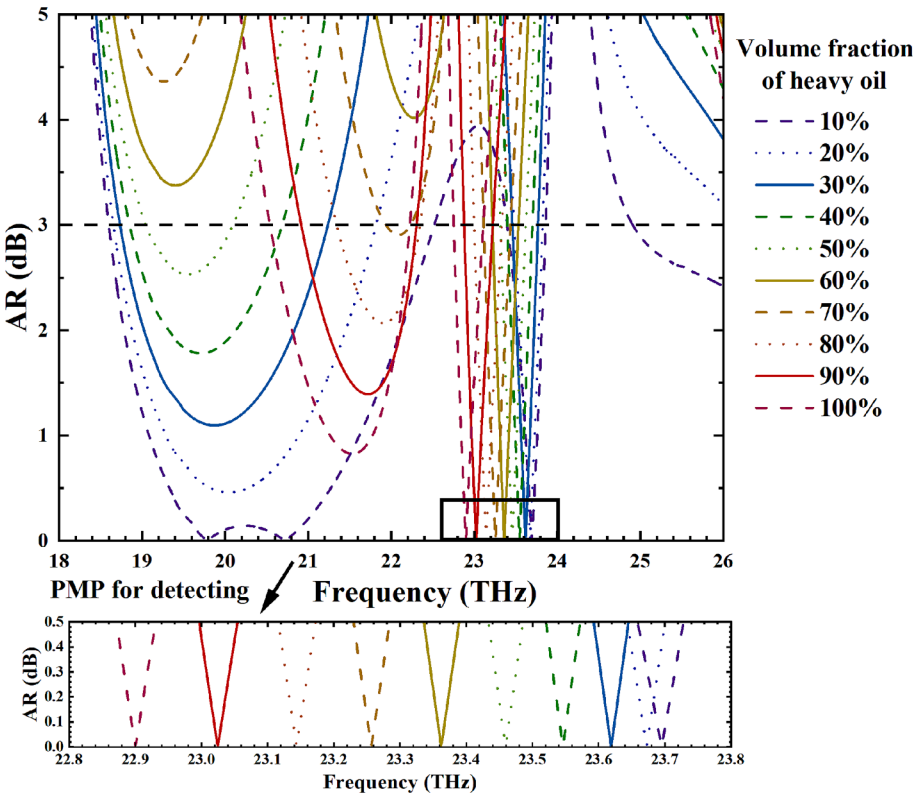

Fig. 7. Curves of AR versus frequency at different volume fractions (from 0 % to 100 %) of heavy oil, and shifting trend of PMP.

absorptance can be generated by a unit phase change, with the VP exhibiting the max S value.

As detailed in Section 2, it is possible to define the phase difference between the TM and TE waves as $\Delta\varphi = \varphi_{TM} - \varphi_{TE}$. For the sake of simplicity, this paper focuses on the application of VPs in detecting functions, and therefore only the polarized form of the EW exiting along the $+z$ direction is considered. As shown in Fig. 3, the operating properties of the VP, when the signal EW is incident with a 45° LPW, are investigated (see Fig. 1).

Fig. 3(a) illustrates the relationship between the phase difference between the TM and TE waves when the + 45° LPW is incident through the VP. Within the coherent polarization conversion band (CPCB), $\Delta\varphi$ remains about 90° difference. In Fig. 3(b), the plot illustrates the variation of the AR with frequency, bounded within a 3 dB range. The VP system exhibits remarkable capabilities in achieving ultra-wideband CPPC from 19.04 to 24.36 THz. Moreover, it demonstrates the generation of mutually chiral CPW outputs within this frequency range. It is also worth noting that in the CPCB, the system has 3 PMPs with AR of exactly 0 dB, which can be regarded as CPPC. The detecting application of PMPs will be explained below. As shown in Fig. 3(c), the output EW intensity of the VP operating in different modes illustrates that in the operating frequency band, the VP has almost no loss of the intensity of the EWs, which reflects the extremely high *PCR*.

3.2. The implementation of the detecting function of CPPC

In this section, the principle of CPPC is used to realize the measurement of salt concentration, temperature, and oil content of seawater. Therefore, the specific parameters of seawater elements can be obtained from Refs.[31–34], where the effect of the seawater conductivity is not taken into account.

Utilizing the CPPC method, the measurements of volume fraction of heavy oil and salt concentration are realized as shown in Fig. 4(a). In this measurement method, we take advantage of variations in the local phase caused by changes in the external environment, which causes a change in the polarization standing wave, thus producing a change in the frequency at the perfect match point. As a result, the variation of external environmental parameters and the frequency of the perfect match point form a bijective relationship, which enables the sensing of seawater volume fraction of heavy oil and salt concentration. In principle, the use of this principle to achieve sensing is highly innovative; essentially, the VP cleverly exploits the sensitivity of the coherent polarization standing waves formed to changes in external parameters to achieve sensing and is therefore specific for use as a detector.

Considering that the seawater to be detected is a two-phase liquid, as displayed in Fig. 4(b), the method of adsorption of porous material is contemplated to be used to realize the detection of oil content by measuring the RI before and after adsorption using the Lichtennecher method for two-phase liquids. Petroleum with a density ranging from 0.943 g/cm^3 to 1 g/cm^3 at a temperature of 15.6 °C and a pressure of 1 atmosphere is classified as heavy oil [31]. On the other hand, petroleum products with a density lower than this range are categorized as light petroleum. The distinction in density plays a significant role in determining the type and properties of petroleum products. Herein, the RI for pure heavy oil is about 1.52. After polymer porous material adsorption, seawater salinity concentration and temperature can be detected [32].

Considering the RI of seawater can be greatly affected by the effect of environmental factors such as salinity concentration C_s in %, temperature T in ℃, and wavelength λ in nm, the function, used to calculate the RI of seawater, is described as follows [33]:

$$n(C_s,T,\lambda) = 1.3104 + \left(1.7799\times10^{-4} - 1.05\times10^{-6}T\right)C_s + 1.6\times10^{-8}T^2C_s - 4382\times\lambda^{-2} - 2.02\times10^{-6}T^2 + \frac{15.868 + 0.01155C_s - 0.00423T}{\lambda} + \frac{1.1455\times10^{-6}}{\lambda^3} \quad (23)$$

To calculate the RI of two-phase compounds, the Lichtennecher method can be employed [31].

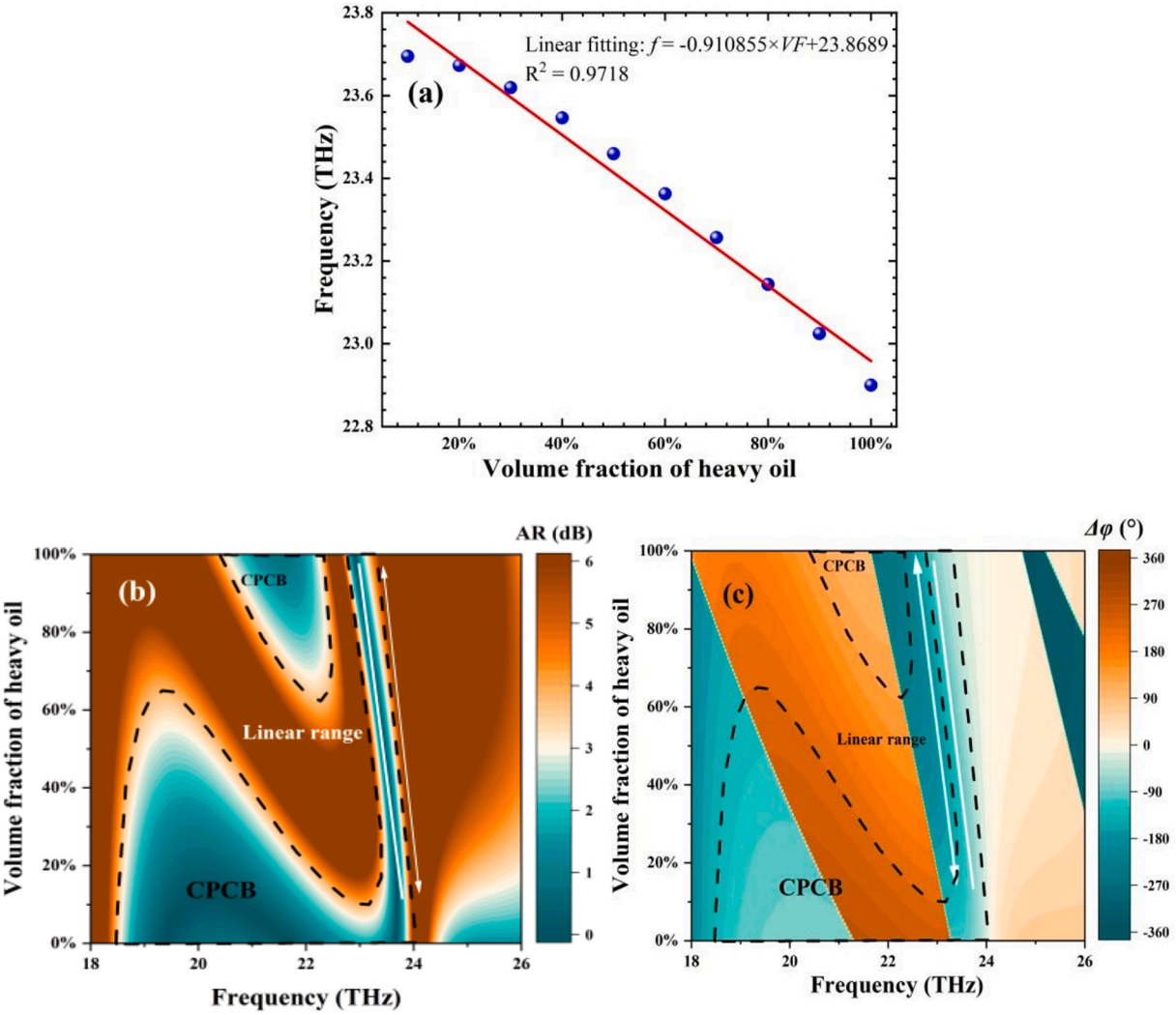

Fig. 8. VP performance in volume fraction of heavy oil detecting. **(a)** The linear fitting curve for the volume fraction and frequency. **(b)** Effects of changes AR with different *VF*. **(c)** Effects of changes in phase difference $\Delta\varphi$.

$$\ln n = (\ln n_1 - \ln n_2) \times VF + \ln n_2 \tag{24}$$

where n_1 is the RI of heavy oil, taken as 1.52 [32], n_2 is the RI of seawater, n is the RI of two-phase compounds and *VF* denotes the volume fraction of heavy oil, which is a dimensionless quantity.

As illustrated in Fig. 5, with the increase of salinity concentration, the PMP moves, from 21.904 THz at 0 % to 21.394 THz at 100 %. The major shift in PMP indicates that VPs have a high detection potential.

When VP is used to detect the salinity concentration of seawater, the specific data are shown in Fig. 6. As demonstrated in Fig. 6(b) and (c), the frequency of PMPs varies linearly with the salinity of seawater accordingly. At the frequency of the PMP, the VP outputs exactly a CPW, which illustrates the detecting potential for VP utilizing CPPC. The linear range is labeled in the figure. The linear range reflects a wide measuring range and high sensitivity. Based on PMP, the VP enables salinity detection with a linear fitting equation of f = -0.72054 × C_s + 21.7, which indicates a high *S*-value of 0.721 THz/%. The curve maintains a good linearity with an R^2 of 0.9997, which reflects the good performance of the detection.

When VP is utilized to detect the volume fraction of heavy oil, the PMP for detection is selected as 25.052 THz for pure seawater. Since the movement of the PMP is more pronounced as the volume fraction of heavy oil changes, this represents a higher sensitivity for VP measurements.

As indicated in Fig. 7, as the volume fraction of heavy oil increases, the PMP redshifts, from 25.052 THz at 0 % to 24.469 THz at 50 % to 23.808 THz at 100 %. The enormous shift in PMP suggests the good detecting potential for VPs.

As displayed in Fig. 8(b) and (c), during coherent optical transmission, PMP appears to have a good linear range from 0 % to 100 %, which is advantageous for detecting and reflects the wide measuring range and high sensitivity. Fig. 8(a) shows the linear fitting curve. A negative correlation exists between the frequency and the volume fraction of heavy oil. With the linear range of 0 %~100 %, the fitting equation is f = -0.910855 × *VF* + 23.8689, with the calculated R^2 being 0.9718. One can learn that the VP is sensitive to the variation of the volume fraction of heavy oil, with an *S* being 0.911 THz/%.

By observing the variations of the PMP, the CPPC method is a brand new way to introduce the detection function to the VP, which owns great potential in the fields of electromagnetic detection and polarization conversion [21]. However, there are some obvious limitations in the detection based on PMP. Firstly, the PMP is generated from the CPPC method, meaning that the realization of the PMP detection needs two coherent EWs working together. Thence, higher requirements are needed for the EWs used. Moreover, given that the VP is based on a P-T symmetric structure and demands the fulfillment of the CPPC, the VP, unlike the traditional single-port detection, must ensure the two ports working simultaneously [5,21], which will increase the difficulty and

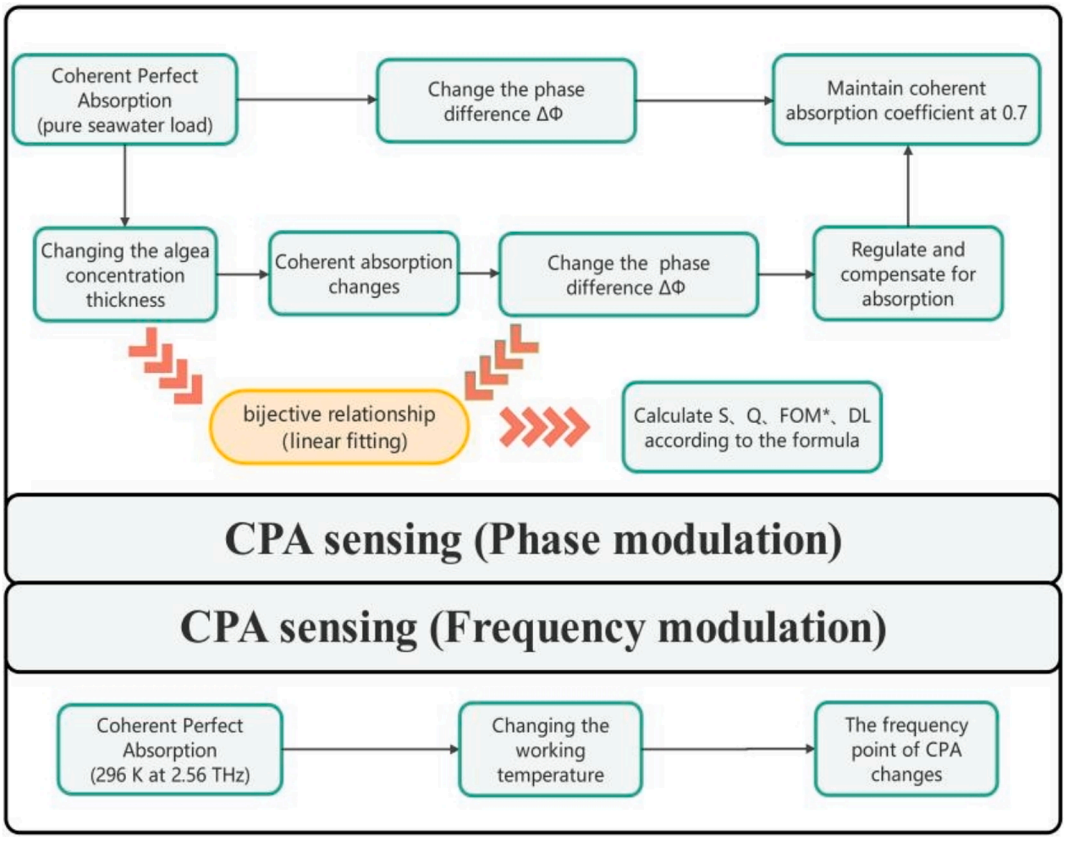

Fig. 9. The exact process of CPA detection under phase modulation and frequency modulation when detecting the concentration of algae.

Table 1
The mean value of the RI of different phytoplankton at different partial water volumes [34].

V_w	0	0.6	0.8
Coccolithophorids	1.562	1.424	1.381
Dinoflagellates	1.552	1.420	1.379
Brown flagellates	1.548	1.419	1.378
Red algae	1.545	1.418	1.378
Blue-green algae	1.541	1.416	1.377
Diatoms	1.538	1.415	1.377
Green algae	1.535	1.414	1.376
Mean value	1.542	1.417	1.377
Standard deviation	0.023	0.009	0.004

complexity of device manufacturing.

For the measurements of the volume fraction of heavy oil and salt concentration, the coherent EWs take the ordinary mode for electromagnetic detection, whose detection performance S is not very ideal. Hence, it is necessary to improve the S to attain a more excellent detection effect. Unfortunately, the idea of applying the VP to detection is first presented, where this paper focuses on the general pattern of EWs and does not take the other modes into account. For the improvement of the S, the EWs modes become the first consideration. The Tamm state and Topological edge state can be combined with the CPPC method to optimize the S of the VP [35,36].

Based on the CPPC method, the measurements of volume fraction of heavy oil and salt concentration are detailedly described above, which utilizes variations in the local phase caused by changes in the external environment. Essentially, with the observation of the PMP changes, the CPPC approach is the detection of the RI variations of the samples pending testing, where the local phase can be altered by the changes in the RI for the tested samples. Therefore, the CPPC method can be applied to the measurement when the tested sample has an RI change, meaning the observation of the PMP shift has a wide detecting range such as pressure, glucose, cancer cells, and so on [37–39].

3.3. The implementation of the detecting function of CPA

Utilizing the structural nature of the VP, phase modulation was employed to make measurements of seawater algal content. Here, V_w denotes partial water volume that is employed to indicate the concentration of algae. Innovatively, phase modulation to compensate for absorption is utilized to measure algae content in seawater. The exact process is shown in Fig. 9.

As shown in Fig. 9, due to the fragility of CPAs, even small changes in physical quantities can lead to significant decreases in uptake. Also, the unit phase shift was found to produce the largest fluctuation in absorbance around absorbance 0.8. Therefore, the use of an optical phase was considered to maintain an absorbance of 0.8. By measuring the phase of an EW, the value of the physical quantity can be calculated. Then, to obtain a numerical relationship between the phase difference and the physical quantity, it is crucial to calculate the value of the phase difference corresponding to different wavelengths repeatedly. In addition, a frequency modulation scheme is proposed by utilizing the sensitivity of the frequency of CPA points to external parameters. In this approach, a bijection is formed between the phase/frequency and the physical quantity, which facilitates increasing the sensitivity of the detecting function [34].

When measuring algae concentrations, it is essential to find common patterns in their refractive indices because of the abundance of algae in the oceans. The average refractive index of algae under different partial water volumes V_w can be found by the content of different species of algae, after averaging them and fitting them. Table 1 demonstrates the mean value of the RI of different phytoplankton at different partial water volumes [34]. Based on the standard deviation, it can be observed that

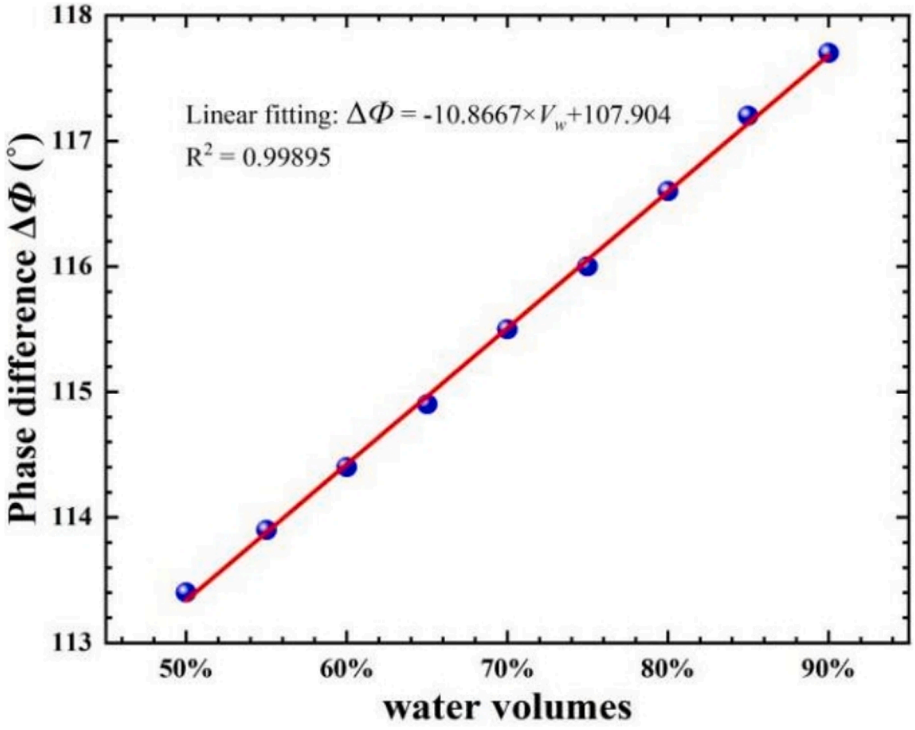

Fig. 10. The linear connection between the phase difference and water volumes under phase modulation detection.

Table 2
The parameters when detecting algal concentrations utilizing CPA detection under phase modulation.

Linear range	*S*	*Q*	*FOM**	*DL*
50 %~90 %	10.8667°/%	4654.24	19757.64 $\%^{-1}$	2.53×10^{-6} %

this method generalizes the refractive indices of different algae very well and the correlation is very high.

In the range of V_w of 50 %~90 %, the average RI of seawater can be described by [34]

$$\overline{n} \approx 1.533 - 0.194 \times V_w \tag{25}$$

Fig. 10 depicts the linear fitting relationship concerning phase difference and water volumes and phase difference shows a negative correlation with water volumes. With an R^2 of 0.99895, the fitting curve is $\Delta\Phi = -10.8667 \times V_w + 107.904$. The parameters when detecting algal concentrations utilizing CPA detection are shown in Table 2. The VP has an exceptionally high sensitivity with *S*, *Q*, and *FOM** values of 10.8667°/%, 4654.24, and 19757.64 $\%^{-1}$, respectively. Simultaneously, the VP has a very small detection error, whose *DL* is as low as 2.53×10^{-6} %. This reflects the excellent detecting function of VP, which has a very broad application prospect in the field of marine ecological detection and other fields.

When it comes to temperature detection under frequency modulation, as illustrated in Fig. 11, with the temperature increases, the CPA point shifts from 2.1 THz at 278 K to 2.9 THz at 308 K. It can be found that measuring temperature using frequency modulation in VP is highly sensitive by the sensitivity property of the frequency point of CPA to temperature changes.

Fig. 12 demonstrates the linear relationship between the frequency of CPA points and different temperatures. The fitting curve is $f = 0.02627 \times T\text{-}5.20788$, with a high R^2 of 0.9992. The parameters when detecting temperature utilizing CPA detection are shown in Table 3. The VP shows excellent performance with *S*, *Q*, and *FOM** values of 0.02627 THz/K, 4654.24, and 47.764 K^{-1}, respectively. Besides, the VP has a relatively small *DL* when utilizing frequency modulation detection of CPA sensing, which indicates a small detection error.

Finally, to systematically visualize the impact of novelty, Table 4 summarizes the polarization conversion and their performance in detecting applications [40–44] and multifunctional detectors [45,46]. By comparison, it is observed that VP maintains a high sensitivity in detection using CPPC and CPA [40–44]. In addition, in contrast to the previously proposed multifunctional detectors, the VP is more practical, has more functions, and has excellent performance [45,46]. It can be found that the previous detection based on polarization transformation is quite different from the formation mechanism of VP, and the principle of coherence is not used. In this paper, a CPPC-based VP capable of detecting the nature of seawater is designed. By comparison, VP has a wider polarization conversion bandwidth with higher sensitivity. In addition, multi-physical detecting is a major feature of VP, which enables the detection of various parameters of seawater and has a wide range of application prospects. In addition, VP ingeniously utilized the fragility of CPA and applied phase & frequency modulation, which is innovative for the measurement of seawater algal concentrations. In addition, a feasible fabrication process and method for VP is provided, which can be found in Supplementary Material.

4. Conclusions

In this paper, the concept of VP is pioneered. Based on the structure of InSb and graphene layers, VP can realize the chiral polarization control of coherent EWs. For transport properties, VP maintains a high *PCR* and ultra-wide operating band and plays a very important role in the manipulation of EW. Herein, the VP is tunable and the size of the VP is not limited by operating wavelength. Utilizing the response of PMPs to seawater, it is possible to detect the salt concentration and volume fraction of heavy oil in seawater. Meanwhile, under TM mode, the CPA was observed at 2.5598 THz, enabling the detection of marine algae and temperature, and the sensitivity of the VP was greatly improved using phase & frequency modulation. Combining the two detection methods, the VP is equipped to realize the full range of detecting capabilities at

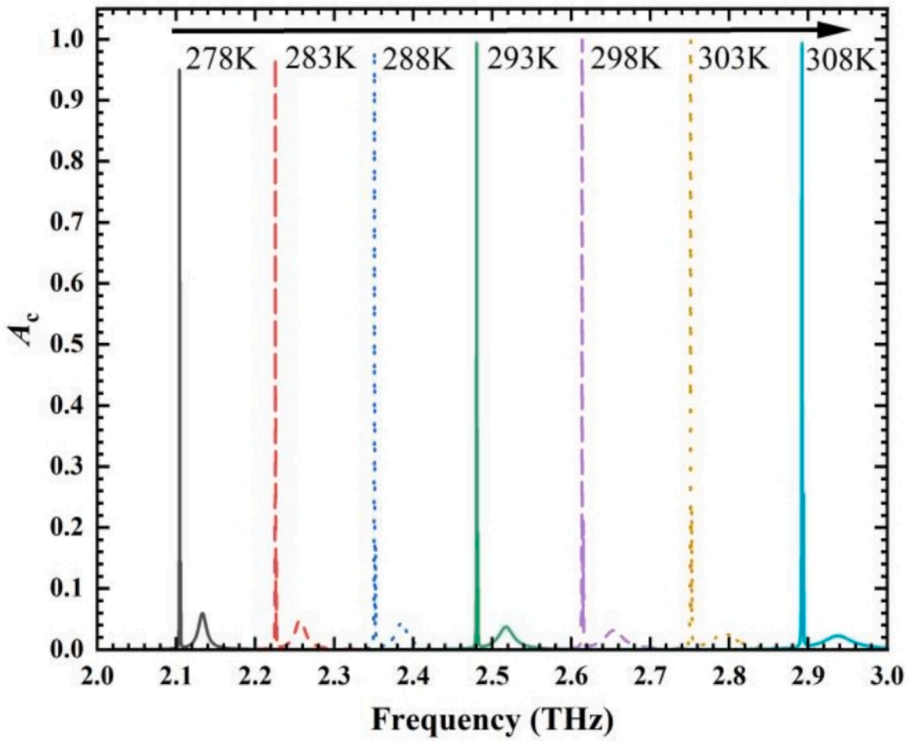

Fig. 11. Curves of A_c versus frequency at different temperatures, and shifting trend of CPA point.

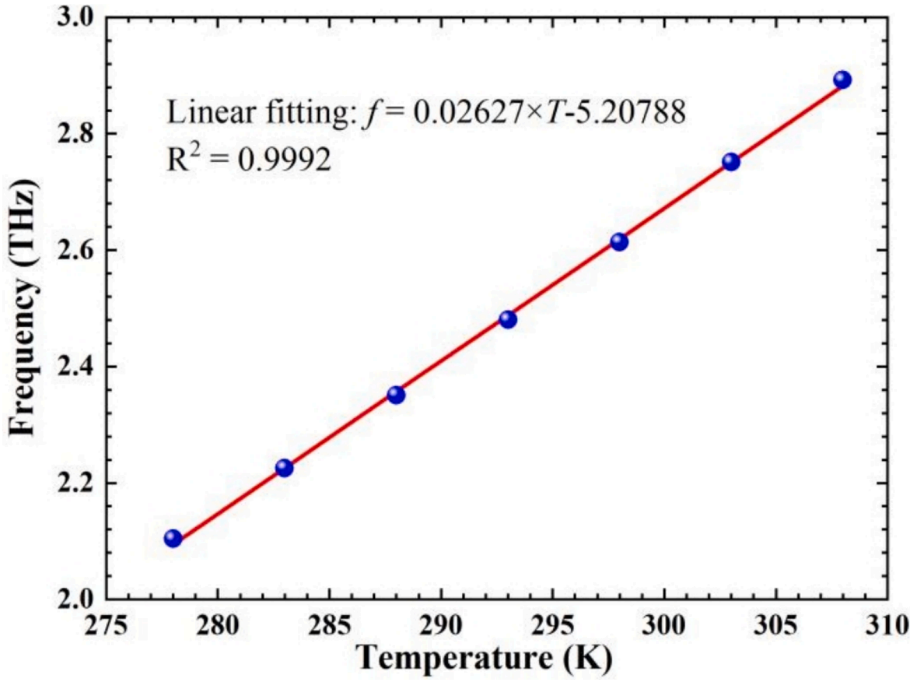

Fig. 12. The linear relationship between the frequency difference and temperatures under frequency modulation detection.

Table 3
The parameters when detecting temperature utilizing CPA detecting under frequency modulation.

Linear range	*S*	*Q*	*FOM**	*DL*
278 ~ 308 K	0.02627 THz/K	4654.24	47.764 K^{-1}	1.04×10^{-3} K

multiple scales. Therefore, VP plays a very important role in marine ecological detection, antenna sensing, propagation, and communication and has a wide range of application prospects.

CRediT authorship contribution statement

Chuan-Qi Wu: Writing – original draft, Validation, Funding acquisition, Formal analysis. **You-ran Wu:** Validation, Software, Resources,

Table 4
Comparision of related research focused on polarization conversion and detecting applications.

Refs.	Function	Conversion Frequency	CPPC	Detecting range	Sensitivity
[40]	Virus detecting	1 ~ 2 THz	×	1 ~ 1.5	N/A
[41]	Anhydrous alcohol	4 ~ 6 THz	×	1 ~ 1.6	1.074 THz/RIU
[42]	magnetic nanoparticles concentration	0.5 ~ 1 THz	×	1.0 ~ 1.9	0.223 THz/RIU
[43]	RI detecting	1.25 ~ 1.75 THz	×	1.0 ~ 2.0	0.066 THz/RIU
[44]	RI detecting	1.65 ~ 1.95 THz	×	1.0 ~ 2.0	0.465 THz/RIU
[45]	RI detecting	×	×	1.333 ~ 1.374	0.454 nm/K
	Temperature detecting		×	293 K ~ 313 K	178.7 nm/RIU
[46]	RI detecting	×	×	1.333 ~ 1.3953	3341.65 nm/RIU
	Temperature detecting		×	323 K ~ 373 K	2.02 nm/K
Our work	Salinity concentration	19.04 ~ 24.35 THz	√	0 ~ 100 %	0.721 THz/%
	Heavy oil			0 ~ 100 %	0.911 THz/%

Methodology. **Hai-Feng Zhang:** Writing – review & editing, Supervision, Project administration, Conceptualization.

Funding

This work was supported by the National College Students Innovation and Entrepreneurship Training Program (Grant No.202310293015Z).

Declaration of competing interest

The authors declare that they have no known competing financial interests or personal relationships that could have appeared to influence the work reported in this paper.

Appendix A. Supplementary material

Supplementary data to this article can be found online at https://doi.org/10.1016/j.measurement.2025.116983.

Data availability

Data will be made available on request.

References

[1] D.G. Baranov, A. Krasnok, T. Shegai, A. Alù, Y. Chong, Coherent perfect absorbers: linear control of light with light, Nat. Rev. Mater. 2 (2017) 1–14.
[2] S.K. Gupta, Y. Zou, X.Y. Zhu, M.H. Lu, L.J. Zhang, X.P. Liu, Y.F. Chen, Parity-time symmetry in non-Hermitian complex optical media, Adv. Mater. 32 (2020) 1903639.
[3] W. Wan, Y. Chong, L. Ge, H. Noh, A.D. Stone, H. Cao, Time-reversed lasing and interferometric control of absorption, Science 331 (2011) 889–892.
[4] Y. Chong, L. Ge, H. Cao, A.D. Stone, Coherent perfect absorbers: time-reversed lasers, Phys. Rev. Lett. 105 (2010) 053901.
[5] Y.R. Wu, R.Y. Dong, J.H. Zou, H.F. Zhang, Advanced optical terahertz fingerprint sensor based on coherent perfect absorption, Phys. Chem. Chem. Phys. 25 (2023) 14257–14265.
[6] S.A. Mousavi, E. Plum, J. Shi, N.I. Zheludev, Coherent control of optical polarization effects in metamaterials, Sci. Rep. 5 (2015) 8977.
[7] M. Kang , Y. D. Chong, Coherent optical control of polarization with a critical metasurface, Phys Rev A. 92(2015). 043826.
[8] G. Pirruccio, M. Ramezani, S.-R.-K. Rodriguez, J.G. Rivas, Coherent control of the optical absorption in a plasmonic lattice coupled to a luminescent layer, Phys. Rev. Lett. 116 (2016) 103002.
[9] D.G. Baranov, A. Krasnok, A. Alu, Coherent virtual absorption based on complex zero excitation for ideal light capturing, Optica 4 (2017) 1457–1461.
[10] Z. Zhang, M. Kang, X. Zhang, X. Feng, Y. Xu, X. Chen, A. Alù, Coherent perfect diffraction in metagratings, Adv. Mater. 32 (2020) 2002341.
[11] M.A. Sofi, K. Saurav, S.K. Koul, Frequency-selective surface-based compact single substrate layer dual-band transmission-type linear-to-circular polarization converter, IEEE Trans. Microwave Theory Tech. 68 (2020) 4138–4149.
[12] D. Liu, B. Huang, L. Yang, J. Wu, N. Li, L. Miao, C. Zhao, Widely tunable narrow linewidth dual-wavelength Yb-doped fiber laser with inhomogeneous polarization output, J. Lightwave Technol. 41 (2023) 327–332.
[13] J. Hao, Y. Yuan, L. Ran, T. Jiang, J.A. Kong, C.T. Chan, L. Zhou, Manipulating electromagnetic wave polarizations by anisotropic metamaterials, Phys. Rev. Lett. 99 (2007) 063908.
[14] F. Xing, H. Chen, S. Xie, J. Yao, Ultrafast surface imaging with an increased spatial resolution based on polarization-division multiplexing, J. Lightwave Technol. 33 (2015) 396–402.
[15] M. Amin, O. Siddiqui, M. Farhat, Polarization-state modulation in fano resonant graphene metasurface reflector, J. Lightwave Technol. 39 (2021) 7869–7875.
[16] Y. Zheng, J. Li, Y. Liu, Y. Li, S. Qu, Novel torsion sensor based on the interaction between modal interference and polarization interference, J. Lightwave Technol. 42 (2024) 2513–2521.
[17] L. Ma, Q. Mao, F. Fan, W. Shi, S. Chang, Polarization control of terahertz waves based on metallic parallel-plate waveguides, J. Lightwave Technol. 42 (2024) 251–257.
[18] F. Wu, M. Chen, S. Xiao, Wide-angle polarization selectivity based on anomalous defect mode in photonic crystal containing hyperbolic metamaterials, Opt. Lett. 47 (2022) 2153–2156.
[19] L. Zagaglia, S. Zanotti, M. Minkov, M. Liscidini, D. Gerace, L. Claudio Andreani, Polarization states and far-field optical properties in dielectric photonic crystal slabs, Opt. Lett. 48(2023) 5017-5020.
[20] Y. She, D. Liu, J. Li, M. Yao, Y. Zheng, F. Wu, Tunable wide-angle high-efficiency polarization selectivity based on a one-dimensional photonic crystal containing elliptical metamaterials, Phys. Lett. 494 (2024) 129299.
[21] Y.R. Wu, R.Y. Dong, H.F. Zhang, Virtual polarizer: coherent perfect ultrawideband polarization control of chiral electromagnetic waves, IEEE Trans. Antennas Propag. 72 (2024) 4370–4382.
[22] D. Vigneswaran, N. Ayyanar, M. Sharma, M. Sumathi, M. Rajan, K. Porsezian, Salinity sensor using photonic crystal fiber, Sensor Actuat. A-Phys. 269 (2018) 22–28.
[23] M. Amiri, M. Abolhasan, N. Shariati, J. Lipman, Remote water salinity sensor using metamaterial perfect absorber, IEEE Trans. Antennas Propag. 70 (2022) 6785–6794.
[24] J. Zhu, G. Wang, Measurement of water content in heavy oil with cavity resonator, Results Phys. 18 (2020) 103192.
[25] C. Zhai, Y. Li, S. Wang, J. Xu, Z. Wen, J. Wang, Experimental research on temperature sensing of seawater based on three interferometers incorporated with bow tie fiber, Photonic Sens. 13 (2023) 230413.
[26] M. Huang, Stress effects on the performance of optical waveguides, Int. J. Solids Struct. 40 (2003) 1615–1632.
[27] K. Kato, N. Umemura, Sellmeier equations for GaS and GaSe and their applications to the nonlinear optics in GaS x Se 1–x, Opt. Lett. 36 (2011) 746–747.
[28] L. Qi, Z. Yang, F. Lan, X. Gao, Z. Shi, Properties of obliquely incident electromagnetic wave in one-dimensional magnetized plasma photonic crystals, Phys. Plasmas. 17 (2010) 8.
[29] A. Andryieuski, A.V. Lavrinenko, Graphene metamaterials based tunable terahertz absorber: effective surface conductivity approach, Opt. Express. 21 (2013) 9144–9155.
[30] B. Lin, J.-L. Wu, X.-Y. Da, W. Li, J.-J. Ma, A linear-to-circular polarization converter based on a second-order band-pass frequency selective surface, Appl. Phys. A-Mater. 123 (2017) 1–5.
[31] Y. Liu, D. Zhu, Z. Yang, N. Ning, Z. Xu, D. Lu, A, Zhang, Relationship between the effective refractive index and pore ratio of nano-porous polymer film, Nano-Optics and Nano-Structures. 4923(2002) 80-84.
[32] P. Cherukupally, W. Sun, A.P. Wong, D.R. Williams, G.A. Ozin, A.M. Bilton, C. B. Park, Surface-engineered sponges for recovery of crude oil microdroplets from wastewater, Nat. Sustain. 3 (2020) 136–143.
[33] X. Quan, E.S. Fry, Empirical equation for the index of refraction of seawater, Appl. Opt. 34 (1995) 3477–3480.
[34] E. Aas, Refractive index of phytoplankton derived from its metabolite composition, J. Plankton Res. 18 (1996) 2223–2249.
[35] Z.A. Zaky, A.M. Ahmed, A.S. Shalaby, A.H. Aly, Refractive index gas sensor based on the Tamm state in a one-dimensional photonic crystal: theoretical optimisation, Sci. Rep. 10 (2020) 9736.
[36] S. Elshahat, Z.E.A. Mohamed, M. Almokhtar, C. Lu, High tunability and sensitivity of 1D topological photonic crystal heterostructure, J. Opt. 24 (2022) 035004.
[37] A.H. Aly, B.A. Mohamed, M. Al-Dossari, D. Mohamed, S.K. Awasthi, M. Sillanpää, Ultra-sensitive pressure sensing capabilities of defective one-dimensional photonic crystal, Sci. Rep. 13 (2023) 18876.
[38] H.A. Elsayed, A. Mehaney, A new method for glucose detection using the one dimensional defective photonic crystals, Mater. Res. Express 6 (2018) 036201.

[39] S. Khani, M. Hayati, Optical biosensors using plasmonic and photonic crystal band-gap structures for the detection of basal cell cancer, Sci. Rep. 12 (2022) 5246.
[40] M. Amin, O. Siddiqui, H. Abutarboush, M. Farhat, R. Ramzan, A THz graphene metasurface for polarization selective virus sensing, Carbon 176 (2021) 580–591.
[41] Y. Hao, R. Yang, Fano resonance-induced high-purity circularly polarized spectra for high-precision refractive index sensing from hybrid resonator-graphene meta-surfaces, Opt. Express 31 (2023) 3059–3071.
[42] F. Fan, C. Zhong, Z. Zhang, S. Li, S. Chang, Terahertz chiral sensing and magneto-optical enhancement for ferromagnetic nanofluids in the chiral metasurface, Nanoscale Adv. 3 (2021) 4790–4798.
[43] M. Islam, J. Sultana, M. Biabanifard, Z. Vafapour, M. Nine, A. Dinovitser, C. Cordeiro, W.-H. Ng, D. Abbott, Tunable localized surface plasmon graphene metasurface for multiband superabsorption and terahertz sensing, Carbon 158 (2020) 559–567.
[44] W. Cen, T. Lang, J. Wang, M. Xiao, High-Q Fano terahertz resonance based on bound states in the continuum in all-dielectric metasurface, Appl. Surf. Sci. 575 (2022) 151723.
[45] Y. Zhao, X.-G. Li, L. Cai, Y.-N. Zhang, Measurement of RI and temperature using composite interferometer with hollow-core fiber and photonic crystal fiber, IEEE Trans. Instrum. 65 (2016) 2631–2636.
[46] Z. Gao, Y. Feng, H. Chen, Q. Chen, Y. Li, M. Zhang, Refractive index and temperature sensing system with high sensitivity and large measurement range using an optical fiber, IEEE Trans. Instrum. 72 (2023) 1–6.